The influence of laser characteristics on internal flow behaviour in laser melting of metallic substrates

Ebrahimi, Amin; Sattari, Mohammad ; Bremer, Scholte J.L.; Luckabauer, Martin; Römer, Gert-willem R.B.E.; Richardson, I.M.; Kleijn, C.R.; Hermans, M.J.M.

DOI
10.1016/j.matdes.2022.110385

Publication date
2022

Document Version
Final published version

Published in
Materials & Design

Citation (APA)
Ebrahimi, A., Sattari, M., Bremer, S. J. L., Luckabauer, M., Römer, G. R. B. E., Richardson, I. M., Kleijn, C. R., & Hermans, M. J. M. (2022). The influence of laser characteristics on internal flow behaviour in laser melting of metallic substrates. *Materials & Design*, *214*, Article 110385. https://doi.org/10.1016/j.matdes.2022.110385

Materials & Design 214 (2022) 110385

Contents lists available at ScienceDirect

Materials & Design

journal homepage: www.elsevier.com/locate/matdes

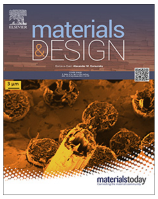

The influence of laser characteristics on internal flow behaviour in laser melting of metallic substrates

Amin Ebrahimi [a,*], Mohammad Sattari [b], Scholte J.L. Bremer [b], Martin Luckabauer [b],
Gert-willem R.B.E. Römer [b], Ian M. Richardson [a], Chris R. Kleijn [c], Marcel J.M. Hermans [a]

[a] *Department of Materials Science and Engineering, Faculty of Mechanical, Maritime and Materials Engineering, Delft University of Technology, Mekelweg 2, 2628CD Delft, The Netherlands*
[b] *Department of Mechanics of Solids, Surfaces and Systems, Faculty of Engineering Technology, University of Twente, Drienerlolaan 5, 7522NB Enschede, The Netherlands*
[c] *Department of Chemical Engineering, Faculty of Applied Sciences, Delft University of Technology, van der Maasweg 9, 2629HZ Delft, The Netherlands*

HIGHLIGHTS

- High-fidelity simulations are performed to predict melt-pool behaviour in laser-based manufacturing.
- An enhanced laser absorption model is used that eliminates the need to calibrate the value of absorptivity.
- The effect of changes in the local energy absorption on the physics of internal flow in laser material processing is explained.
- The difference between melt-pool shapes obtained using different laser sources are described.
- The validity and reliability of the model in predicting the melt-pool shape are demonstrated.

ARTICLE INFO

Article history:
Received 7 October 2021
Revised 27 December 2021
Accepted 4 January 2022
Available online 5 January 2022

Keywords:
Laser melting
Laser beam absorption
Melt pool behaviour
Welding and additive manufacturing
Numerical simulation

GRAPHICAL ABSTRACT

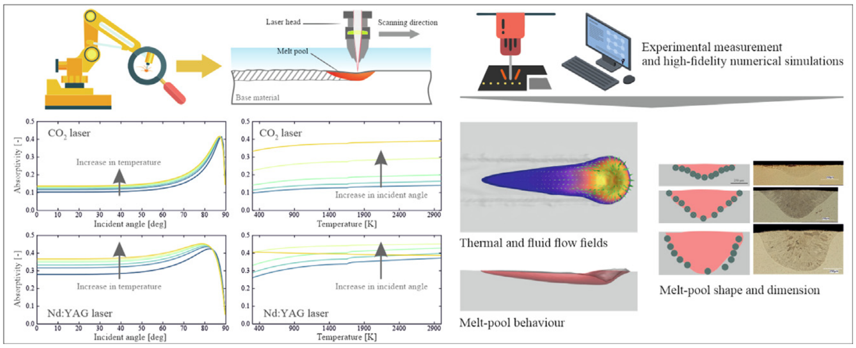

ABSTRACT

The absorptivity of a material is a major uncertainty in numerical simulations of laser welding and additive manufacturing, and its value is often calibrated through trial-and-error exercises. This adversely affects the capability of numerical simulations when predicting the process behaviour and can eventually hinder the exploitation of fully digitised manufacturing processes, which is a goal of "industry 4.0". In the present work, an enhanced absorption model that takes into account the effects of laser characteristics, incident angle, surface temperature, and material composition is utilised to predict internal heat and fluid flow in laser melting of stainless steel 316L. Employing such an absorption model is physically more realistic than assuming a constant absorptivity and can reduce the costs associated with calibrating an appropriate value. High-fidelity three-dimensional numerical simulations were performed using both variable and constant absorptivity models and the predictions compared with experimental data. The results of the present work unravel the crucial effect of absorptivity on the physics of internal flow in laser material processing. The difference between melt-pool shapes obtained using fibre and CO_2 laser sources is explained, and factors affecting the local energy absorption are discussed.

---

* Corresponding author.
E-mail address: A.Ebrahimi@tudelft.nl (A. Ebrahimi).

https://doi.org/10.1016/j.matdes.2022.110385
0264-1275/

1. Introduction

Laser-beam melting of metallic substrates forms the basis of many advanced fusion-based manufacturing processes (such as laser welding, laser cladding, laser metal deposition (LMD), and selective laser melting (SLM)) and has brought new perspectives on advancement of materials processing and manufacturing of high-integrity products. Successful adoption of laser-beam melting in real-world engineering applications requires finding processing windows within which the product quality should meet the intended standards [1]. However, determining the processing window through trial-and-error experiments is challenging and involves significant costs due to the large number of process parameters and the coupling between various physical phenomena. Simulation-based approaches have been recognised as a promising alternative to costly and time-inefficient experiments and can be utilised to reduce the costs of design-space exploration [2,3]. Moreover, numerical simulations can enhance our understanding of the complex transport phenomena in laser material processing that are not easily accessible through experiments [4,5].

Successful adoption of simulation-based approaches for process development and optimisation relies predominantly on adequate modelling of various physical phenomena that occur during laser melting (*e.g.* laser-matter interaction, heat and fluid flow, and solid-liquid phase transformation) [6]. Assumptions made to develop computational models often affect their reliability, accuracy and performance in predicting and describing the process behaviour. For instance, studies suggest that melt-pool surface deformations affect power-density distribution, leading to changes in the thermal field, Marangoni flow pattern and the melt-pool shape [7–9]. Conversely, previous investigations [10–13] have shown a considerable influence of laser characteristics and power-density distribution on molten metal flow behaviour in laser welding and additive manufacturing. Thus, there seems to be an important bi-directional coupling between laser power-density distribution and melt-pool behaviour. Neglecting such effects in numerical simulations of laser-beam melting can negatively affect the quality of numerical predictions of thermal fields, microstructures and properties of the product [8,14]. Moreover, assumptions made to develop a computational model may necessitate the incorporation of unphysical tuning parameters to obtain agreement between numerical and experimental data [8,15]. This can reduce the model reliability for design-space explorations since a change in process parameters or material properties may require recalibrating the tuning parameters [16,17]. Understanding the influence of such assumptions on numerical predictions is therefore essential and can guide the modelling efforts to enhance the current numerical simulations.

Absorption of laser-energy, energy-density distribution and its variation over time are critical components influencing the modelling of laser-beam melting [18] and depend on a variety of process parameters including the characteristics of the laser system (*e.g.* laser intensity and wavelength), thermophysical properties of the material, surface roughness and chemistry, and interactions of the melt-pool surface with the laser beam [19–22]. In the majority of previous studies on laser-beam melting, the absorption of laser energy is assumed to be constant [13], neglecting the unsteady interactions between laser-beam and material surface [23]. Studies have shown that changes in melt-pool surface morphology and temperature can affect the local absorptivity of the material [10,24–26]. The Fresnel absorption model [27], which is commonly employed in numerical simulations of laser melting (particularly when the ray-tracing method is used), accounts for the effects of laser-ray incident angle and material refractive index, but neglects the temperature dependence of material absorptivity [20]. In laser melting of metallic substrates, the material often experiences large changes in temperature that can significantly affect the thermophysical properties of the material, including the material absorptivity [28,29]. Moreover, the complex molten metal flow in melt-pools continuously disturbs temperature distribution over the surface [8], affecting the local absorptivity of the material. The Fresnel model cannot reflect the variation of local energy absorption that occurs due to changes in melt-pool surface temperature [12,30,31]. Hence, the Fresnel model cannot describe variations in material absorptivity with sufficient accuracy, particularly in cases where the melt-pool surface deformations are small compared to the melt-pool depth (for instance, laser cladding, conduction-mode laser welding and laser metal deposition).

Realising that in practical applications the laser type is not a control parameter, as commercial machines come with a fixed laser type, the present work focuses on understanding the influence of laser characteristics on complex heat and molten metal flow in laser-beam melting. Such an understanding allows us to explain, for example, the difference between melt-pool shapes obtained using fibre transmissible and CO_2 lasers (*i.e.* the most widely employed lasers for industrial applications). High-fidelity three-dimensional numerical simulations are performed using an enhanced laser-beam absorption model that takes into account the effects of laser characteristics, surface temperature, incident angle and base-material composition. The results obtained using the enhanced absorption model for different laser systems and laser powers are compared with those obtained using a constant absorptivity and factors affecting the local energy absorption are discussed. Additionally, experiments are carried out for different laser powers to validate the melt-pool shapes predicted using the present computational model. The results and discussions provided in the present work guide the modelling efforts to improve simulations of fusion-based welding and additive manufacturing.

2. Problem description

As shown in Fig. 1, a moving laser beam is employed to locally heat and melt the substrate that is made of a stainless steel alloy (AISI 316L) and is initially at an ambient temperature of 300 K. The gas layer above the plate is included in simulations to track the motion of gas-metal interface. The influence of laser characteristics on melting of a metallic substrate is studied numerically for fibre and CO_2 lasers, whose wavelengths are different. The laser beam is perpendicular to the substrate surface and has a Gaussian intensity profile.

Three batches of three-dimensional numerical simulations are executed for different laser types and powers using both constant and variable absorptivity models to describe the complex thermal and fluid flow fields in the melt pool. For cases where the absorptivity is assumed to be constant, different values of the absorptivity are examined, as reported in Table 1. The dimensions of the computational domain defined in a Cartesian coordinate system, and the boundary conditions applied to the outer boundaries, are shown in Fig. 1. Heat input from the laser, heat losses due to convection, radiation and vaporisation, as well as forces acting on the melt pool (*i.e.* Marangoni shear force, capillary force, and recoil pressure) are implemented in the simulations by adding source and sink terms to the governing equations, as described in Section 3. Although the thermal buoyancy force is often negligible compared with Marangoni force in driving the molten metal flow in laser melting [8], a variable density model is employed in the present work to account for thermal buoyancy force as well as the solidification shrinkage. Temperature-dependent material

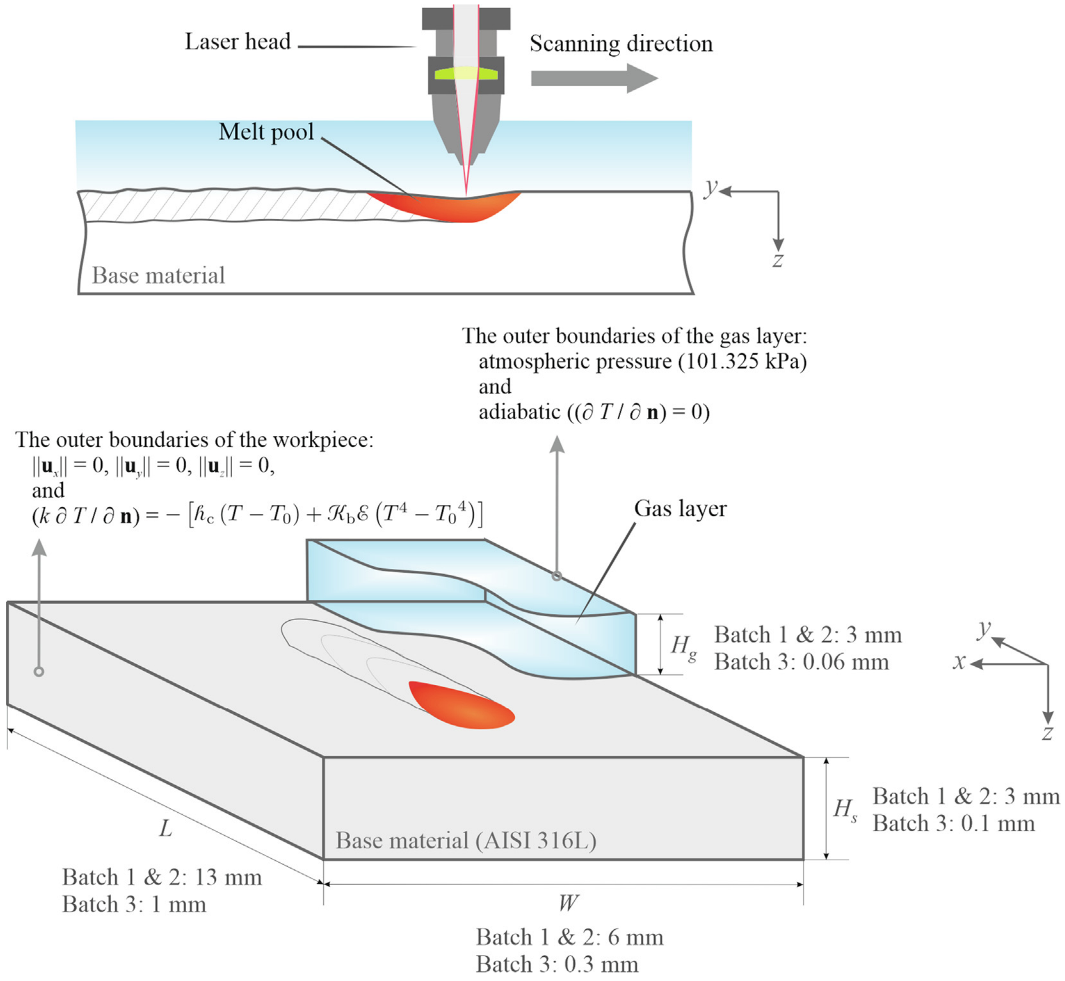

Fig. 1. Schematic of laser melting, dimensions of the computational domain and the mathematical expressions used for the boundary conditions. Parts of the gas layer are clipped for visualisation.

Table 1
Summary of the process parameters studied in the present work.

Parameter	Batch 1	Batch 2	Batch 3
Laser type	CO_2 laser	Nd:YAG laser	Fibre laser[a]
Laser power $\mathscr{P}$ [W]	900–2100 (interval: 300)	500–900 (100)	200
Wavelength λ [m]	1.060×10^{-5}	1.064×10^{-6}	1.070×10^{-6}
Constant absorptivity α [–]	0.10–0.14 (0.02) and 0.18	0.3–0.4 (0.05)	0.3–0.4 (0.05)
Travel speed $\mathscr{V}$ [ms^{-1}]	10^{-2}	10^{-2}	1.5
Spot size (D4σ) d_b [m]	2×10^{-3}	2×10^{-3}	1.1×10^{-4}
Interaction time $t_i = d_b/\mathscr{V}$ [s]	0.2	0.2	7.3×10^{-5}

[a] Continuous wave fibre laser (YLR-500-AC, IPG Photonics) [1].

Table 2
Material properties employed in the present work.

Property	Stainless steel (AISI 316L)	Gas (argon) [33]
Density ρ [kg m^{-3}]	see Fig. 2	1.623
Specific heat capacity c_p [J kg^{-1} K^{-1}]	see Fig. 2	520.64
Thermal conductivity k [W m^{-1} K^{-1}]	see Fig. 2	1.58×10^{-2}
Dynamic viscosity μ [kg m^{-1} s^{-1}]	see Fig. 2	2.12×10^{-5}
Molar mass M [kg mol^{-1}]	5.58×10^{-2} [34]	3.9948×10^{-2}
Latent heat of fusion $\mathscr{L}_f$ [J kg^{-1}]	2.7×10^{5} [34]	–
Latent heat of vaporisation $\mathscr{L}_v$ [J kg^{-1}]	7.45×10^{6} [35]	–
Solidus temperature T_s [K]	1658 [34]	–
Liquidus temperature T_l [K]	1723 [34]	–
Boiling temperature T_b [K]	3086 [36]	–

properties are employed for both the solid and the molten metal in the present numerical simulations and the values are reported in Table 2 and Fig. 2. Although the properties of argon are also temperature-dependent, they have been assumed to be constant in the present work for the sake of simplicity, see Table 2. This assumption is made based on the fact that the density, viscosity and thermal conductivity of argon are very small compared to those of the metal, therefore variations of those gas properties with temperature have negligible influence on the numerical predictions [32].

3. Methods

3.1. Model formulation

The present computational model is developed on the basis of the finite-volume approach and utilises the volume-of-fluid (VOF) method [40] to locate the gas-metal interface. It is assumed that both the molten metal and argon are Newtonian fluids and that their densities are pressure-independent. Based on these

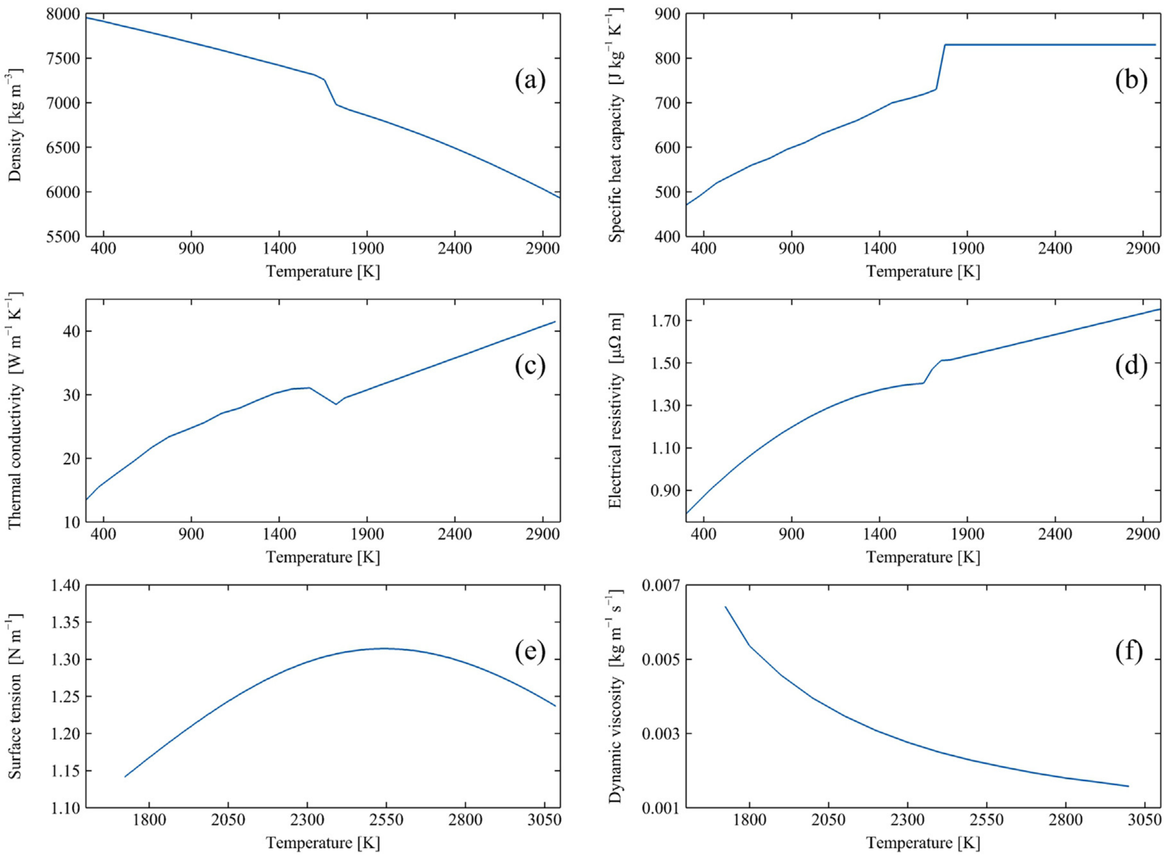

Fig. 2. Temperature-dependent properties of stainless steel 316L. (a) density [37], (b) specific heat capacity [34], (c) thermal conductivity [34], (d) electrical resistivity [38] (e) surface tension [39] and (f) dynamic viscosity [37].

assumptions, the governing equations for conservation of mass, momentum and energy as well as for the advection of the scalar function ϕ, which represents the local volume-fraction of the steel phase in a computational cell, are defined as follows:

$$\frac{D\rho}{Dt} + \rho(\nabla \cdot \mathbf{u}) = 0, \tag{1}$$

$$\rho \frac{D\mathbf{u}}{Dt} = \mu \nabla^2 \mathbf{u} - \nabla p + \mathbf{F}_\mathrm{d} + \mathbf{F}_\mathrm{s}, \tag{2}$$

$$\rho \frac{Dh}{Dt} = \frac{k}{c_\mathrm{p}} \nabla^2 h - \rho \frac{D(\psi \mathscr{L}_\mathrm{f})}{Dt} + S_\mathrm{q} + S_\mathrm{l}, \tag{3}$$

$$\frac{D\phi}{Dt} = 0. \tag{4}$$

Here, ρ is the density, t the time, $\mathbf{u}$ the fluid velocity vector, μ the dynamic viscosity, p the pressure, h the sensible heat, k the thermal conductivity, c_p the specific heat capacity, and $(\psi \mathscr{L}_\mathrm{f})$ the latent heat with ψ being the local liquid volume-fraction and $\mathscr{L}_\mathrm{f}$ the latent heat of fusion. It is assumed that the liquid volume-fraction ψ varies linearly with temperature [41], and its value is calculated as follows:

$$\psi = \frac{T - T_\mathrm{s}}{T_\mathrm{l} - T_\mathrm{s}}; \quad T_\mathrm{s} \leqslant T \leqslant T_\mathrm{l}. \tag{5}$$

The effective material properties in computational cells were computed as follows:

$$\xi = \phi \xi_\mathrm{m} + (1 - \phi) \xi_\mathrm{g}, \tag{6}$$

where, ξ corresponds to density ρ, specific heat capacity c_p, thermal conductivity k or viscosity μ, and subscripts 'm' and 'g' indicate metal or gas respectively.

$\mathbf{F}_\mathrm{d}$ is a sink term incorporated into Eq. (2) to damp fluid velocities in the mushy region and to suppress them in solid regions, and is defined based on the enthalpy-porosity technique [42] as

$$\mathbf{F}_\mathrm{d} = -C \, \frac{(1 - \psi)^2}{\psi^3 + \epsilon} \, \mathbf{u}, \tag{7}$$

where, C is the permeability coefficient (also known as the mushy-zone constant) and ϵ is a constant, equal to 10^{-3}, employed to avoid division by zero. The value of the permeability coefficient C was set to 10^7 kg m^{-2} s^{-2}, based on the criteria proposed by Ebrahimi et al. [43].

A continuum surface force model [44] is used to model forces acting on the gas-metal interface (*i.e.* capillary force, Marangoni shear force and recoil pressure). Accordingly, the source term $\mathbf{F}_\mathrm{s}$ is incorporated into Eq. (2) as follows:

$$\mathbf{F}_\mathrm{s} = \mathbf{f}_\mathrm{s} \|\nabla \phi\| \frac{2\rho}{\rho_\mathrm{m} + \rho_\mathrm{g}}, \tag{8}$$

where, $\mathbf{f}_\mathrm{s}$ is the surface force applied to a unit area, and the term $2\rho/\left(\rho_\mathrm{m} + \rho_\mathrm{g}\right)$ is included to redistribute the surface-forces towards the heavier phase. The surface force $\mathbf{f}_\mathrm{s}$ is determined as follows:

$$\begin{aligned} \mathbf{f}_\mathrm{s} &= \mathbf{f}_\mathrm{capillary} + \mathbf{f}_\mathrm{Marangoni} + \mathbf{f}_{\mathrm{P}_\mathrm{recoil}} \\ &= \gamma \kappa \hat{\mathbf{n}} + \tfrac{\mathrm{d}\gamma}{\mathrm{d}T} [\nabla T - \hat{\mathbf{n}}(\hat{\mathbf{n}} \cdot \nabla T)] + \left[0.54 \cdot p_0 \exp\left(\tfrac{\mathscr{L}_\mathrm{v} M \, (T - T_\mathrm{b})}{\mathrm{R} \, T \, T_\mathrm{b}}\right)\right] \hat{\mathbf{n}}. \end{aligned} \tag{9}$$

where, γ is the surface tension, $\hat{\mathbf{n}}$ the surface unit normal vector ($\hat{\mathbf{n}} = \nabla\phi/\|\nabla\phi\|$), κ the surface curvature ($\kappa = \nabla \cdot \hat{\mathbf{n}}$), p_0 the ambient pressure, and R the universal gas constant. The third term on the right-hand side of Eq. (9), $\mathbf{f}_{\mathrm{P_{recoil}}}$, is included to model the recoil pressure generated due to vaporisation of the molten metal [45,46].

The source S_q and the sink term S_l are incorporated into Eq. (3) to model the laser heat input to the material and heat losses from the material due to convection, radiation and vaporisation respectively, and are defined as follows:

$$S_\mathrm{q} = \mathscr{F}_\mathrm{q}\left[\frac{2\,\mathscr{a}\,\mathscr{P}}{\pi r_\mathrm{b}^2}\exp\left(\frac{-2\,\mathscr{R}^2}{r_\mathrm{b}^2}\right)\|\nabla\phi\|\frac{2\,\rho\,c_\mathrm{p}}{(\rho\,c_\mathrm{p})_\mathrm{m}+(\rho\,c_\mathrm{p})_\mathrm{g}}\right], \tag{10}$$

$$S_\mathrm{l} = -\left(S_\mathrm{convection}+S_\mathrm{radiation}+S_\mathrm{vaporisation}\right)\|\nabla\phi\|\frac{2\,\rho\,c_\mathrm{p}}{(\rho\,c_\mathrm{p})_\mathrm{m}+(\rho\,c_\mathrm{p})_\mathrm{g}}. \tag{11}$$

Here, $\mathscr{a}$ is the absorptivity, $\mathscr{P}$ the laser power, r_b the radius of the laser beam, $\mathscr{R}$ the radial distance from the laser-beam axis in x-y plane, and

$$S_\mathrm{convection} = \mathscr{h}_\mathrm{c}(T - T_0), \tag{12}$$

$$S_\mathrm{radiation} = \mathscr{K}_\mathrm{b}\mathscr{E}\left(T^4 - T_0^4\right), \tag{13}$$

$$S_\mathrm{vaporisation} = 0.82\cdot\frac{\mathscr{L}_\mathrm{v}M}{\sqrt{2\pi M\mathrm{R}T}}\,p_0\exp\left(\frac{\mathscr{L}_\mathrm{v}M\,(T-T_\mathrm{b})}{\mathrm{R}\,T\,T_\mathrm{b}}\right), \tag{14}$$

where, T_0 is the ambient temperature, $\mathscr{K}_\mathrm{b}$ the Stefan-Boltzmann constant, and $\mathscr{h}_\mathrm{c}$ and $\mathscr{E}$ are the heat transfer coefficient and the radiation emissivity equal to 25 W m^{-2} K^{-1} [47] and 0.45 [48] respectively. Compared to the total laser energy absorbed by the material, the heat losses from the material due to convection and radiation are quite small; thus, the precise values of $\mathscr{h}_\mathrm{c}$ and $\mathscr{E}$ are not critical in the present simulations. The coefficient 0.82 in Eq. (14) is included based on Anisimov's theory [45] to account for the reduced cooling effect due to metal vapour condensation.

In the VOF method, the energy fluxes applied to the material surface are included as volumetric source terms in the computational cells that encompass the melt-pool surface (*i.e.* cells with $0 < \phi < 1$). Hence, melt-pool surface deformations that occur during the process can result in an increase in the total heat input to the material [8]. $\mathscr{F}_\mathrm{q}$ in Eq. (10) is a dynamic adjustment factor introduced to abate artificial increase in energy absorption due to surface deformations and is defined as

$$\mathscr{F}_\mathrm{q} = \frac{1}{\iiint\limits_{\forall}\|\nabla\phi\|\frac{2\,\rho\,c_\mathrm{p}}{(\rho\,c_\mathrm{p})_\mathrm{m}+(\rho\,c_\mathrm{p})_\mathrm{g}}\mathrm{d}V}, \tag{15}$$

where, "$\forall$" indicates the computational domain. The influence of utilising such an adjustment factor on numerical predictions of molten metal flow in laser melting is explained by Ebrahimi et al. [8].

3.1.1. Absorptivity model

When a laser beam with total energy of $\mathscr{P}$ interacts with material, here stainless steel 316L, part of its energy is absorbed by the material for a fraction equal to its absorptivity ($\mathscr{a}$). Numerical simulations developed for laser welding and additive manufacturing commonly assume the absorptivity to be constant [36], which is physically unrealistic, and its value is often regarded as a calibration parameter [13]. The absorptivity should be considered as a material property and not a calibration parameter [13]. In the present work, the amount of laser energy absorbed by the material was modelled according to the absorptivity model proposed by Yang et al. [13] and Mahrle and Beyer [11], which takes into account the effects of laser characteristics, laser-ray incident angle, surface temperature and base-material composition. Accordingly, the absorptivity $\mathscr{a}$ for circularly polarised or un-polarised laser radiation was approximated as follows [49]:

$$\mathscr{a} = 1 - \frac{R_\mathrm{s}+R_\mathrm{p}}{2}, \tag{16}$$

where, according to the Fresnel's reflection equations, R_s and R_p are the reflectance for parallel and perpendicularly polarised light [25] defined as

$$R_\mathrm{s} = \frac{\alpha^2+\beta^2-2\alpha\cos(\theta)+\cos^2(\theta)}{\alpha^2+\beta^2+2\alpha\cos(\theta)+\cos^2(\theta)}, \tag{17}$$

$$R_\mathrm{p} = R_\mathrm{s}\left(\frac{\alpha^2+\beta^2-2\alpha\sin(\theta)\tan(\theta)+\sin^2(\theta)\tan^2(\theta)}{\alpha^2+\beta^2+2\alpha\sin(\theta)\tan(\theta)+\sin^2(\theta)\tan^2(\theta)}\right). \tag{18}$$

Here, θ is the incident angle of the laser ray, and α and β are functions of the refractive index n and the extinction coefficient k of the irradiated material. The values of α, β, n and k were determined as follows [13]:

$$\alpha = \left(\frac{\sqrt{\left(n^2-k^2-\sin^2(\theta)\right)^2+4n^2k^2}+n^2-k^2-\sin^2(\theta)}{2}\right)^{\frac{1}{2}}, \tag{19}$$

$$\beta = \left(\frac{\sqrt{\left(n^2-k^2-\sin^2(\theta)\right)^2+4n^2k^2}-n^2+k^2+\sin^2(\theta)}{2}\right)^{\frac{1}{2}}, \tag{20}$$

$$n = \left(\frac{\sqrt{\mathscr{e}_\mathrm{r}^2+\mathscr{e}_\mathrm{i}^2}+\mathscr{e}_\mathrm{r}}{2}\right)^{\frac{1}{2}}, \tag{21}$$

$$k = \left(\frac{\sqrt{\mathscr{e}_\mathrm{r}^2+\mathscr{e}_\mathrm{i}^2}-\mathscr{e}_\mathrm{r}}{2}\right)^{\frac{1}{2}}, \tag{22}$$

where, $\mathscr{e}_\mathrm{r}$ and $\mathscr{e}_\mathrm{i}$ are the real and imaginary parts of the relative electric permittivity $\tilde{\mathscr{e}}$ respectively [50], defined as

$$\mathscr{e}_\mathrm{r} = 1 - \frac{\omega_\mathrm{p}^2}{\mathscr{f}^2+\delta^2}, \tag{23}$$

$$\mathscr{e}_\mathrm{i} = \frac{\delta}{\mathscr{f}}\frac{\omega_\mathrm{p}^2}{\mathscr{f}^2+\delta^2}. \tag{24}$$

Here, $\omega_\mathrm{p}, \mathscr{f}$ and δ are the plasma frequency, laser frequency and damping frequency respectively, defined as follows [11,13]:

$$\omega_\mathrm{p} = \sqrt{\frac{N_\mathrm{e}\,\mathrm{q}_\mathrm{e}^2}{\mathrm{M}_\mathrm{e}\,\mathrm{v}_0}}, \tag{25}$$

$$\mathscr{f} = \frac{2\pi\ \mathscr{c}}{\lambda}, \tag{26}$$

$$\delta = \omega_\mathrm{p}^2\,\mathrm{v}_0\,\mathscr{R}_T, \tag{27}$$

where, N_e is the mean number density of free electrons (the value of which approximately equals to $5.83 \times 10^{2}9\ \mathrm{m}^{-3}$ for stainless steel 316L [13]), q_e the elementary electric charge, M_e the electron rest mass, v_0 the electric constant, $\mathscr{c}$ the speed of light in vacuum, λ the emission wavelength of the laser, and $\mathscr{R}_T$ the temperature-dependent electrical resistivity. The values approximated using the present absorptivity model for stainless steel 316L are presented in Fig. 3, showing the influence of laser emission wave-

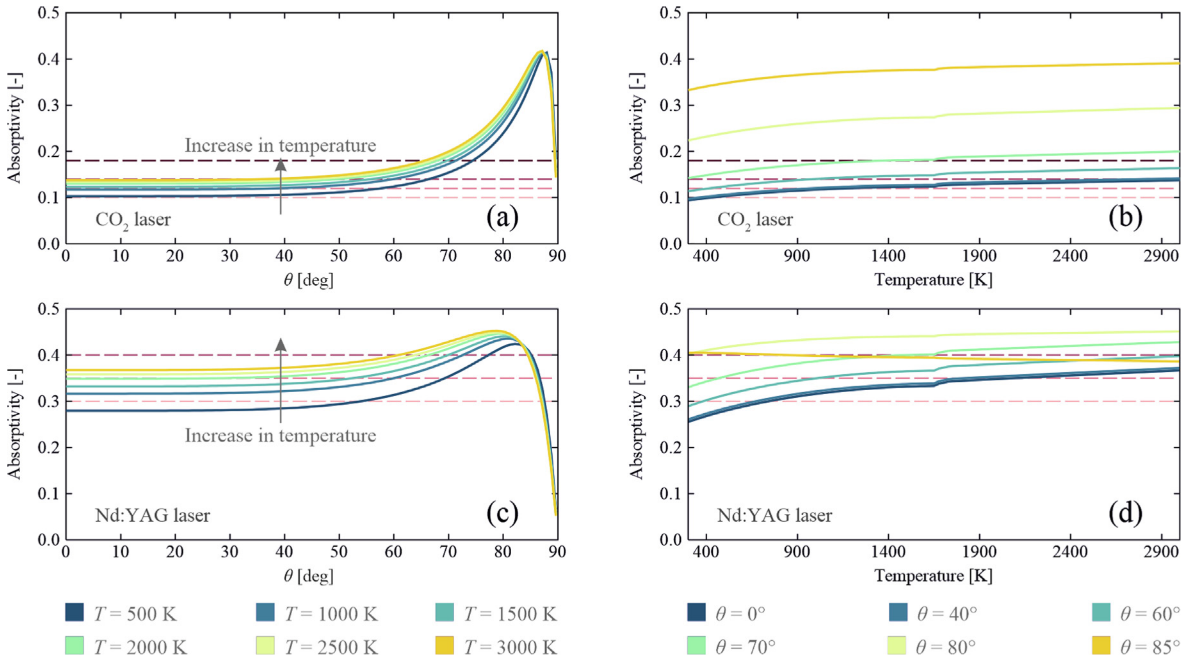

Fig. 3. The effects of laser emission wavelength λ, temperature and incident angle of the laser ray θ on the absorptivity of stainless steel 316L. Values are obtained from the absorptivity model described in Section 3.1.1. (a and b) CO_2 laser with $\lambda = 1.060 \times 10^{-5}$ m and (c and d) Nd:YAG laser with $\lambda = 1.064 \times 10^{-6}$ m. Dashed lines indicate the constant absorptivities studied in the present work.

length, incident angle and temperature on the absorptivity. The data shown in Fig. 3 suggest that the incident angle of the laser ray θ negligibly affects the absorptivity up to 40° but its effect becomes significant for larger incident angles (for instance, in cases where a keyhole is formed). Additionally, changes in the temperature notably affect absorptivity, making the assumption of constant absorptivity questionable.

3.2. Numerical implementation

The present numerical simulations were constructed on the foundation of a proprietary flow solver, ANSYS Fluent [51]. User-defined functions (UDFs) programmed in the C programming language were developed to implement the absorptivity model, source and sink terms in the momentum and energy equations as well as the surface tension model in the simulations. As shown in our previous works [52,8,3,9,53], the numerical grid cell spacing should be chosen to have at least 35 cells in the melt pool region along its width. Accordingly, hexahedral cells were used to discretise the computational domain with minimum cell spacing of 50 μm for cases in batch 1 and 2 (CO_2 and Nd:YAG welds, melt-pool widths of about 1500 μm), and 3 μm for cases in batch 3 (continuous wave fibre laser welds, melt-pool widths of about 100 μm), as shown in Fig. 4. Accordingly, the total number of computational cells is about 1.2×10^6 for cases in batch 1 and 2, and about 1.0×10^6 for cases in batch 3.

The central differencing scheme with second-order accuracy and a first-order implicit scheme were employed for spatial discretisation and time marching respectively. A fixed time-step size Δt was used in the simulations and its value was chosen sufficiently small ($10^{-8}\text{s} < \Delta t < 10^{-5}\text{s}$) to achieve a Courant number ($\text{Co} = \|\mathbf{u}\|\Delta t/\Delta x$) less than 0.2. The PRESTO (pressure staggering option) scheme [54] was used for the pressure interpolation, and the PISO (pressure-implicit with splitting of operators) scheme [55] was used to couple velocity and pressure fields. An explicit compressive VOF method [56] was employed to formulate the advection of the scalar field ϕ. Each simulation was run in parallel on 16 cores (AMD EPYC 7452) of a high-performance computing cluster with 256 GB memory.

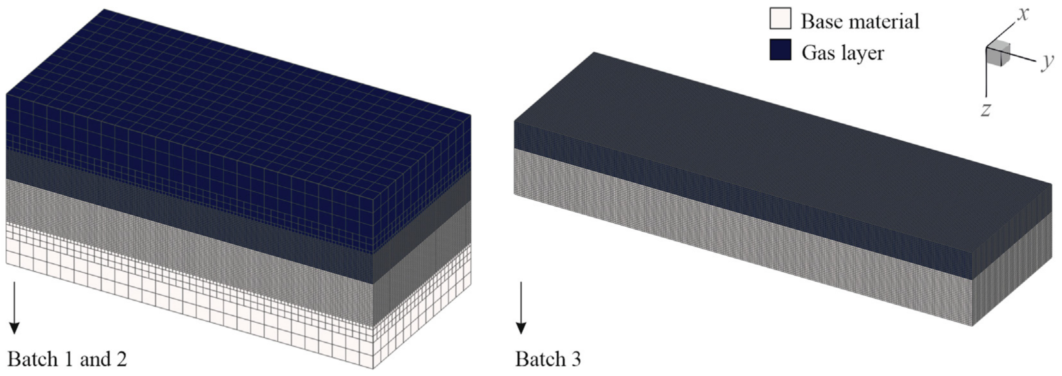

Fig. 4. The computational meshes employed in the present work.

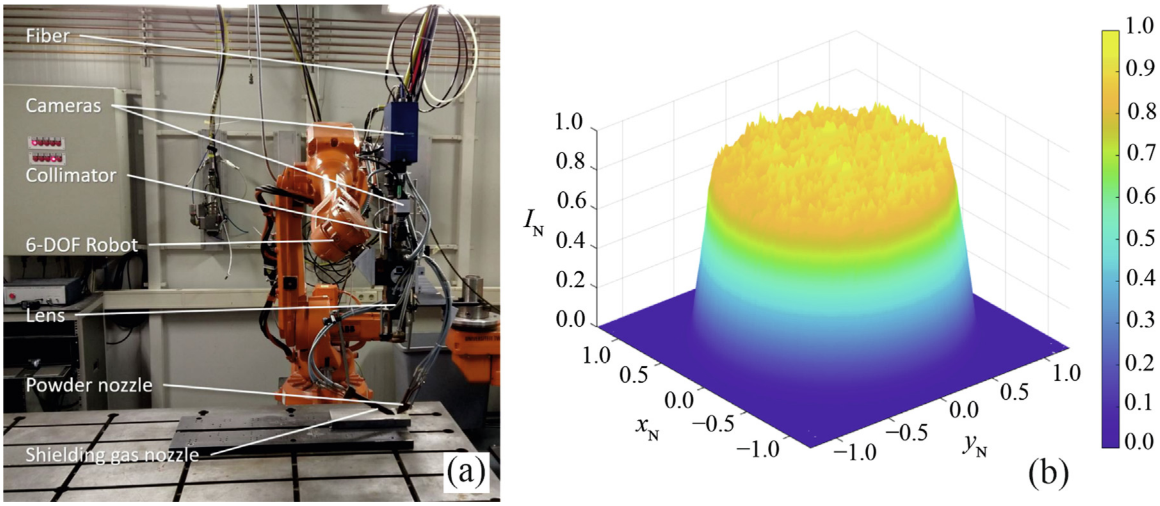

Fig. 5. (a) The experimental setup employed in the present work. (b) Power-density distribution produced using the present experimental setup. In subfigure (b), the power-density profile is normalised with the respective maximum peak, and coordinates are non-dimensionalised using the laser-beam radius r_b.

3.3. Experimental setup and procedure

The experimental setup employed in the present work is shown in Fig. 5. An Yb:YAG disk laser (Trumpf TruDisk 10001) that was connected to a fibre with a core diameter of 6×10^{-4} m was employed. The fibre transports the laser light towards the focusing optics (Trumpf BEO D70), consisting of a 200 mm collimator and 400 mm focusing lens. The focusing optics are mounted to a 6-DOF robot (ABB IRB-2600M2004). Using this setup, a laser spot with a diameter of 1.2 mm and a top-hat power-density distribution was produced (see Fig. 5(b)). Melting tracks with a length of 80 mm were made on an AISI 316L plate with dimensions of 250 mm × 100 mm × 10 mm. The travel speed was set to 20 mm s^{-1}. The melt pool was protected from oxidation during the process using argon gas at a flow rate of about 20 L/min. Each experiment was repeated at least three times to ensure that the results are reproducible. The samples were cut transversely, polished and etched to capture macrographs using a digital microscope (Keyence VHX 7000). A solution of 100 mL HCl, 100 mL H_2O and 10 mL NHO_3 with a temperature of about 310 K was used for etching the samples.

4. Results and discussion

4.1. Model validation

The reliability and accuracy of the present computational model are examined by comparing the numerically predicted melt-pool shapes with those obtained from experiments with different laser systems, laser powers and power-density distributions. To visualise the melt-pool shapes, cross-sectional macrographs were prepared *ex situ* after experiments and iso-surfaces of solidus temperature were projected on the *x-z* plane after numerical simulations. It should be noted that the numerical results were obtained using the variable absorptivity model described in Sectione 3.1.1 without calibration. Fig. 6 shows a comparison between the melt-pool shapes obtained from the present computational model with those obtained from experiments using an Yb:YAG laser ($\lambda = 1.030 \times 10^{-6}$ m) and different laser powers, which indicates a reasonable agreement (generally less than 5% difference in melt-pool dimensions).

The characteristics of the laser system used in laser melting can affect the absorptivity and hence can change the resulting melt-pool shape. The results of the present computational model are also benchmarked against the experimental data reported by Kell et al. [57] for laser melting of a 1 mm-thick steel plate using a CO_2 laser ($\lambda = 1.060 \times 10^{-5}$ m) with the energy-density ($\mathscr{E} = \mathscr{P}/(\mathscr{V} d_b)$) being set to 120 MJ m^{-2}, and the results are shown in Fig. 7. To compare the numerically predicted melt-pool shape with experimental measurements, the relative difference between melt-pool dimensions (*i.e.* the melt-pool width and depth) was calculated as follows:

$$\%\text{Deviation} = \left|\frac{\mathscr{L}_{\text{numerical}} - \mathscr{L}_{\text{experimental}}}{\mathscr{L}_{\text{experimental}}}\right| \times 100, \qquad (28)$$

where, $\mathscr{L}$ indicates the melt-pool depth and width. In this case, the deviation between the numerically predicted and the experimentally measured melt-pool dimensions is less than 2%, demonstrating the reliability of the present computational model in predicting the melt-pool shape. The deviation between the numerical and experimental results can be attributed to uncertainties in modelling temperature-dependent material properties, particularly in the liquid phase, the assumptions made to develop the present computational model as well as uncertainties associated with the experimental measurements.

4.2. Melt-pool shape and dimensions

To be able to systematically study the effects of laser characteristics and melt-pool surface deformations on variation of local absorptivity, three batches of simulations are considered for different laser types. For cases in batch 1 and 2, the power density is too low to cause significant vaporisation and surface deformations are small compared to the melt-pool depth. Thus, changes in the absorptivity for a specific laser and material can be attributed primarily to changes in surface temperature. The laser spot size for the cases in batch 3 is intentionally chosen smaller than that for the cases in batch 1 and 2 to achieve high values of power-density, resulting in significant vaporisation of the material and melt-pool surface deformations compared to its depth. For all three batches, the results obtained using the enhanced absorption model are compared with those obtained using a constant absorptivity. Fig. 8 shows the numerically predicted melt-pool dimensions obtained for different laser powers using CO_2 and Nd:YAG lasers (*i.e.* cases in batch 1 and 2). The melt-pool dimensions obtained using the variable absorptivity model are compared with those

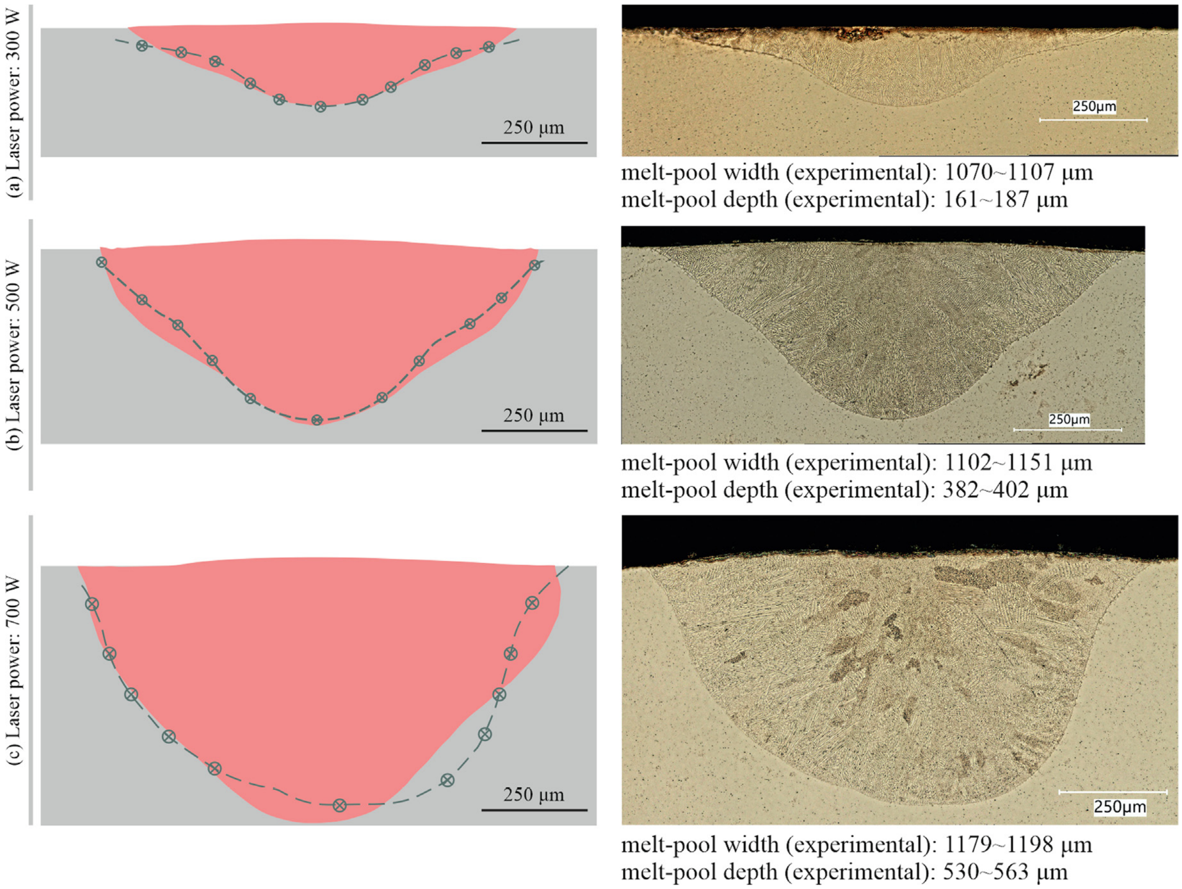

Fig. 6. Numerically predicted melt-pool shapes obtained from the present computational model (left column, regions shaded in pink) compared with the experimental macrographs (right column, circles and dashed lines). The base material is stainless steel 316L. An Yb:YAG laser ($\lambda = 1.030 \times 10^{-6}$ m) was used, the laser beam had a top-hat power-density distribution, the spot size d_b was 1.2 mm and travel speed $\mathscr{V}$ was set to 20 mm s^{-1}. The energy-density ($\mathscr{E} = \mathscr{P}/(\mathscr{V} d_b)$) ranges between 12.5 MJ m^{-2} and 29.2 MJ m^{-2}.

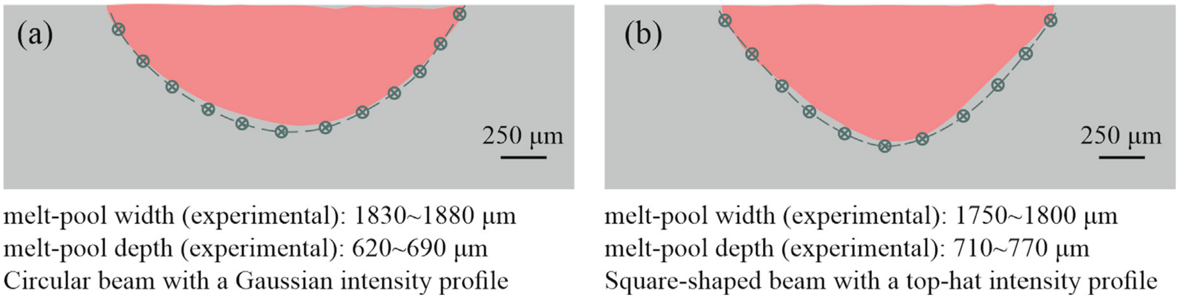

Fig. 7. Comparison of the melt-pool shapes obtained from the present computational model (regions shaded in pink) with the experimental measurements of Kell et al. [57] (circles and dashed line). (a) Circular laser beam with a Gaussian power-density distribution and a spot size (D4σ) of $d_b = 1.25$ mm, and (b) Square-shaped laser beam with a top-hat power-density distribution and a spot size of $d_b = 1.25$ mm. The base material is stainless steel 316L. A CO$_2$ laser ($\lambda = 1.060 \times 10^{-5}$ m) was used and the energy-density ($\mathscr{E} = \mathscr{P}/(\mathscr{V} d_b)$) was set to 120 MJ m^{-2} for both cases.

obtained using different constant values of the absorptivity. For cases in batch 1 and 2, the power density is too low to cause significant vaporisation and surface deformations are small compared to the melt-pool depth. Thus, changes in the absorptivity for a specific laser and material can be attributed primarily to changes in surface temperature (see Fig. 3).

For the cases where the CO$_2$ laser was employed (Fig. 8(a–c)), melt-pool dimensions predicted using a constant absorptivity between 0.12 and 0.14 seem to agree with those obtained using the variable absorptivity model. However, the results suggest that employing a constant absorptivity does not necessarily render all the melt-pool dimensions with the same level of accuracy, which means the results are less reliable with respect to those obtained using the variable absorptivity model. This can be attributed to the fact that changes in local energy absorption due to changes in surface temperature, and changes in total energy absorption over time are both neglected when a constant absorptivity is employed. Surface temperature in the spot region after reaching a quasi-steady-state condition for CO$_2$ laser melting with a laser power of $\mathscr{P} = 2100$ W ranges between 1900 K and 2650 K, resulting in absorptivities that range between 0.130 and 0.136 according to the variable absorptivity model and in agreement with the

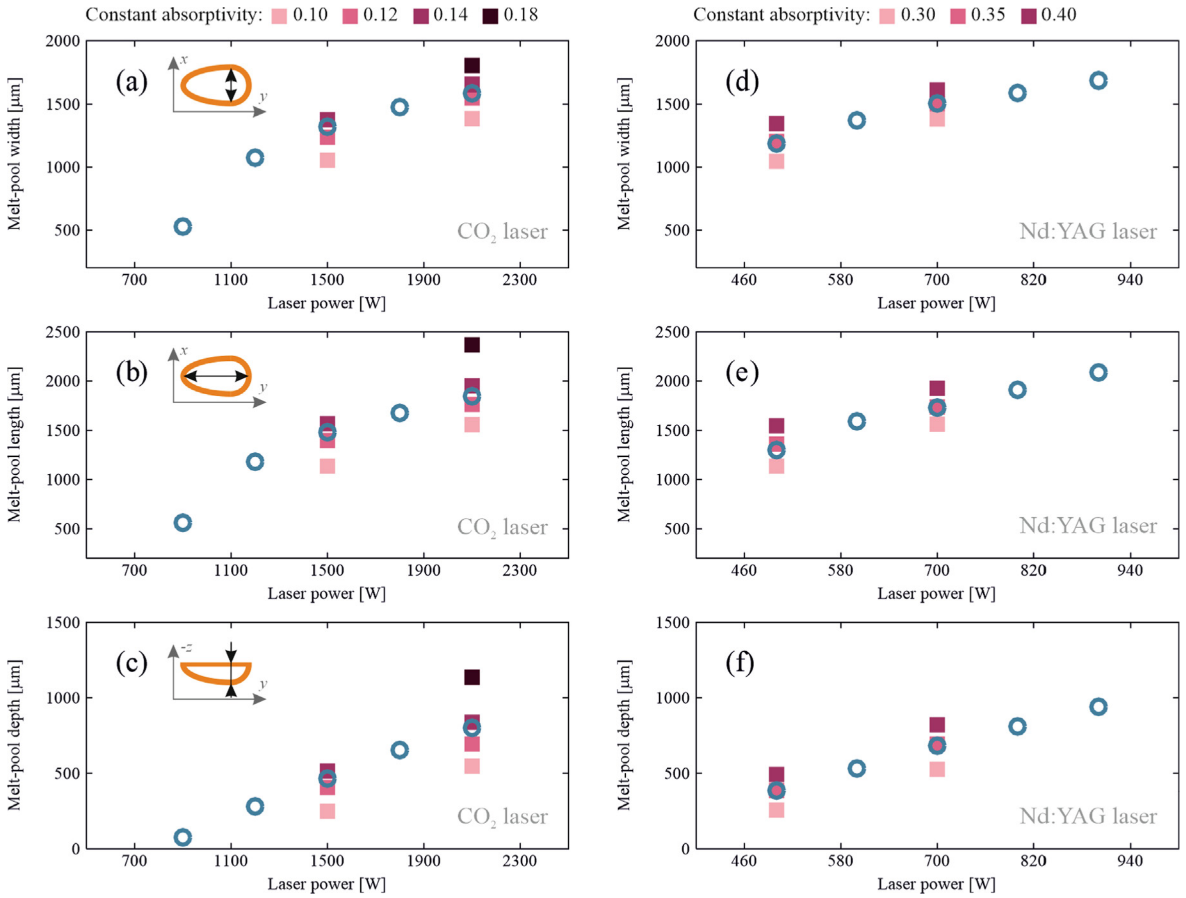

Fig. 8. Melt-pool dimensions obtained from the present computational model using variable absorptivity (circles) and constant absorptivity (squares) for different laser powers and laser systems ((a–c) CO$_2$ laser ($\lambda = 1.060 \times 10^{-5}$ m) and (d–f) Nd:YAG laser ($\lambda = 1.064 \times 10^{-6}$ m)). Travel speed $\mathscr{V}$ was set to 10^{-2} m s^{-1} for all the cases.

results shown in Fig. 8(a–c). Although a good agreement between numerical and experimental melt-pool dimensions might be achievable using a constant absorptivity model, the use of a constant absorptivity requires a *posteriori* fitting of the absorptivity value to the experiments, whereas such a fitting is not required employing the variable absorptivity model described in Section 3.1.1.

The results shown in Fig. 8 suggest that for a certain set of process parameters, a lower laser power is required to obtain a melt-pool with similar dimensions using an Nd:YAG laser with an emission wavelength of $\lambda = 1.064 \times 10^{-6}$ m than a CO$_2$ laser with an emission wavelength of $\lambda = 1.060 \times 10^{-5}$ m. This arises because the absorptivity for a CO$_2$ laser is generally lower than that for an Nd:YAG laser when the incident angle is too small to affect the absorptivity significantly ($\theta < 40^\circ$, as is suggested by the data shown in Fig. 3), which is the case in conduction-mode laser melting. For the cases where the Nd:YAG laser was employed (Fig. 8(d–f)), using a constant absorptivity of 0.35 can render the melt-pool dimensions with a reasonable resolution. When an Nd:YAG laser with a laser power of $\mathscr{P} = 700$ W is employed, numerically predicted surface temperature in the spot region after reaching a quasi-steady-state condition ranges between 1900 K and 2600 K. For this temperature range, the absorptivity varies between 0.347 and 0.36 according to the variable absorptivity model, and its arithmetic average 0.354 is close to 0.35. Since the melt-pool surface temperature and its distribution are not known *a priory* and are significantly influenced by the process parameters as well as the complex internal molten metal flow, running trial-and-error tests is indispensable to calibrate the value of constant absorptivity. Running such trial-and-error tests increases the total costs of computational analyses and such *ad hoc* calibration often lacks generality.

Fig. 9 shows the numerically predicted melt-pool shapes obtained using both variable and constant absorptivity models for a fibre laser with an emission wavelength of $\lambda = 1.070 \times 10^{-6}$ m (*i.e.* cases in batch 3). The power density for the cases in batch 3 is relatively high, resulting in significant vaporisation of the material and melt-pool surface deformations compared to its depth. In contrast to the cases in batch 1 and 2, the absorptivity for the cases in batch 3 are affected by both temperature and incident angle of the laser ray (see Fig. 3).

The results presented in Fig. 9 show an agreement between the melt-pool dimensions predicted using a constant absorptivity of 0.35 and those obtained using the variable absorptivity model. For the cases in batch 3, surface temperature in the laser spot region ranges roughly from 800 K (because of the relatively high travel speed, the material is in the solid state in front part of the laser spot region) to the boiling temperature of 3086 K corresponding to absorptivities between 0.30 and 0.37 (with an arithmetic average of 0.335) based on the variable absorptivity model for $\theta = 0^\circ$. Demonstrably, reducing the absorptivity from 0.35 to 0.335 decreases the total amount of energy absorbed by the material, resulting in smaller melt-pool dimensions than those predicted using the variable absorptivity model. The increase in local energy absorption due to the increase in temperature and laser incident angle is neglected when a constant absorptivity model is employed. For the cases in batch 3, the incident angle of the laser ray θ increases from 0° to 50° with melt-pool surface

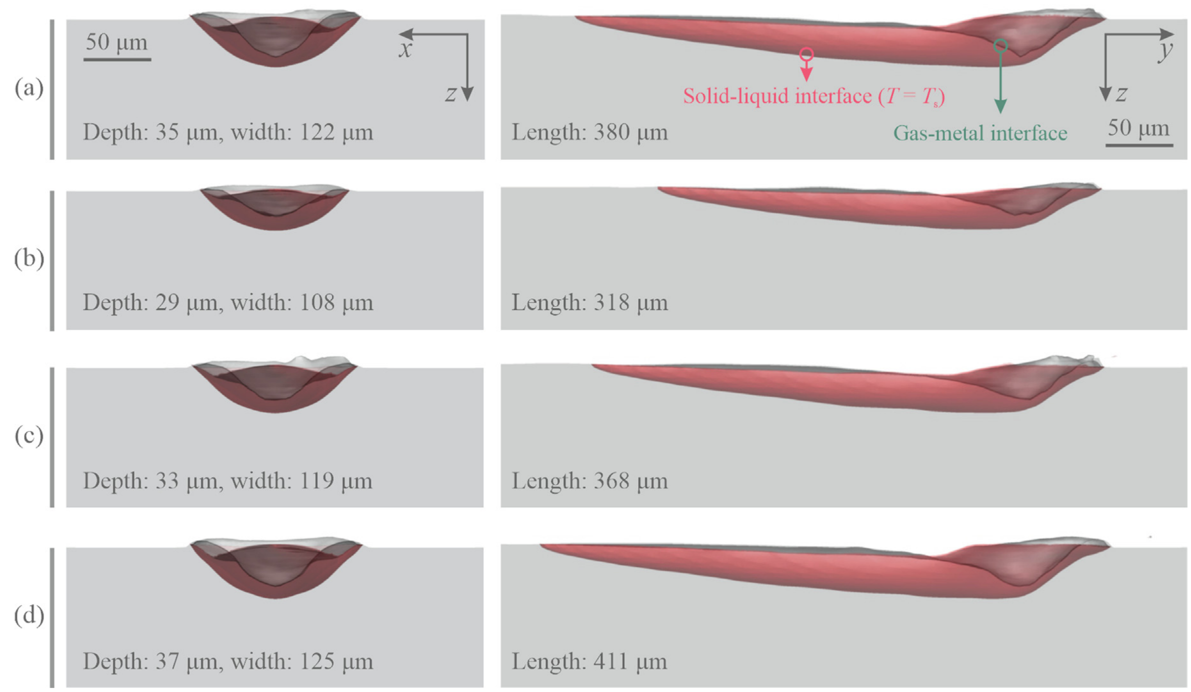

Fig. 9. Melt-pool shapes obtained from the present computational model for different cases in batch 3 (fibre laser ($\lambda = 1.070 \times 10^{-6}$ m), $\mathscr{P} = 200$ W, spot size $d_b = 1.1 \times 10^{-4}$ m and travel speed $\mathscr{V} = 1.5$ m s^{-1}). (a) variable absorptivity, (b) constant absorptivity $\alpha = 0.30$, (c) $\alpha = 0.35$ and (d) $\alpha = 0.40$.

depression, resulting in an increase in the local energy absorption according to the variable absorptivity model and in turn increases the melt-pool surface temperature, which leads to further increase in absorptivity. Eventually, the material reaches the boiling temperature and vaporisation limits further increase of melt-pool surface temperature. Variations of total energy input and energy-density distribution due to dynamic changes of surface temperature and morphology affect material vaporisation and thus the recoil pressure that is responsible for melt-pool surface depression. Consequently, these effects cannot be described adequately when a constant absorptivity model is employed in numerical simulations of laser welding and additive manufacturing. Modelling such phenomena with sufficient accuracy is crucial in numerical simulations of transition from conduction to keyhole mode laser melting as well as those developed to predict solidification microstructure and texture.

4.3. Thermal and fluid flow fields

Soon after exposing the material to laser radiation, a melt pool forms and grows over time and if the boundary conditions allow, reaches a quasi-steady-state condition. Fig. 10 shows the thermal and fluid flow fields over the melt-pool surface at different time instances after reaching the quasi-steady-state condition during laser melting using an Nd:YAG laser ($\lambda = 1.064 \times 10^{-6}$ m) with different laser powers. The temperature gradient induced over the surface generates Marangoni shear forces that drive molten metal flow. The molten metal moves from the cold regions adjacent to the melt-pool rim towards the central part of the pool while absorbing energy from the laser beam. This agrees well with experimental observations and discussions reported by Mills et al. [58] for stainless steel alloys. The absorbed energy advects with the flow and diffuses through the material into the surrounding solid regions. As the material absorbs energy, surface temperature increases and if the power-density is high enough, the surface temperature reaches a critical value at which the sign of the temperature gradient of surface tension ($\mathrm{d}\gamma/\mathrm{d}T$) changes (see Fig. 2(e)), resulting in a change in flow direction. Interactions between the inward and the outward streams result in a complex flow pattern in the pool that is inherently unsteady and three-dimensional [59,8]. Two vortices are observed over the melt-pool surface close to the hot spot, generating an asymmetric flow pattern that fluctuates around the centre-line of the pool. This fluid motion forms a rotational flow pattern in the pool that transfers the absorbed heat from the surface to the bottom of the pool [60]. Because of this rotational fluid motion, an element of molten metal volume may move from one side of the pool to the other side, resulting in a cross-cellular flow [61] that enhances mixing in the pool. Maximum fluid velocity in the pool reach values of about 0.6 m s^{-1}, corresponding to a Péclet number ($\mathrm{Pe} = \rho c_\mathrm{p} \mathscr{D} \|\mathbf{u}\| / k$) in the order of $\mathcal{O}(100)$ that indicates the significant contribution of advection to the total energy transfer. Molten metal flow in the pool disturbs the thermal field and in turn affects the absorptivity and Marangoni forces. A similar flow pattern is observed over the surface when a CO$_2$ laser is employed, and representative results are provided in the supplementary materials.

Fig. 11 shows a time series of numerically predicted thermal and fluid flow fields over the melt-pool surface after reaching the quasi-steady-state condition during laser melting using a fibre laser ($\lambda = 1.070 \times 10^{-6}$ m) with a laser power of $\mathscr{P}$ = 200 W and a travel speed of $\mathscr{V}$ = 1.5 m s^{-1}. In this case, three distinctive regions are identified: a region with significant surface depression under the effect of recoil pressure, a trailing region characterised by low fluid velocities (less than 0.2 m s^{-1}) and temperature (less than 1750 K), and a transition zone in between. A similar choice of subdivision is reported by Khairallah et al. [36] to describe the anatomy of a melt track in selective laser melting of a powder bed, where the surface tension temperature gradient ($\mathrm{d}\gamma/\mathrm{d}T$) was assumed to be a negative constant value. Because of the relatively high laser power-density, surface temperature in the spot region increases rapidly and reaches the boiling temperature T_b, leading to significant material vaporisation and increase in recoil pressure

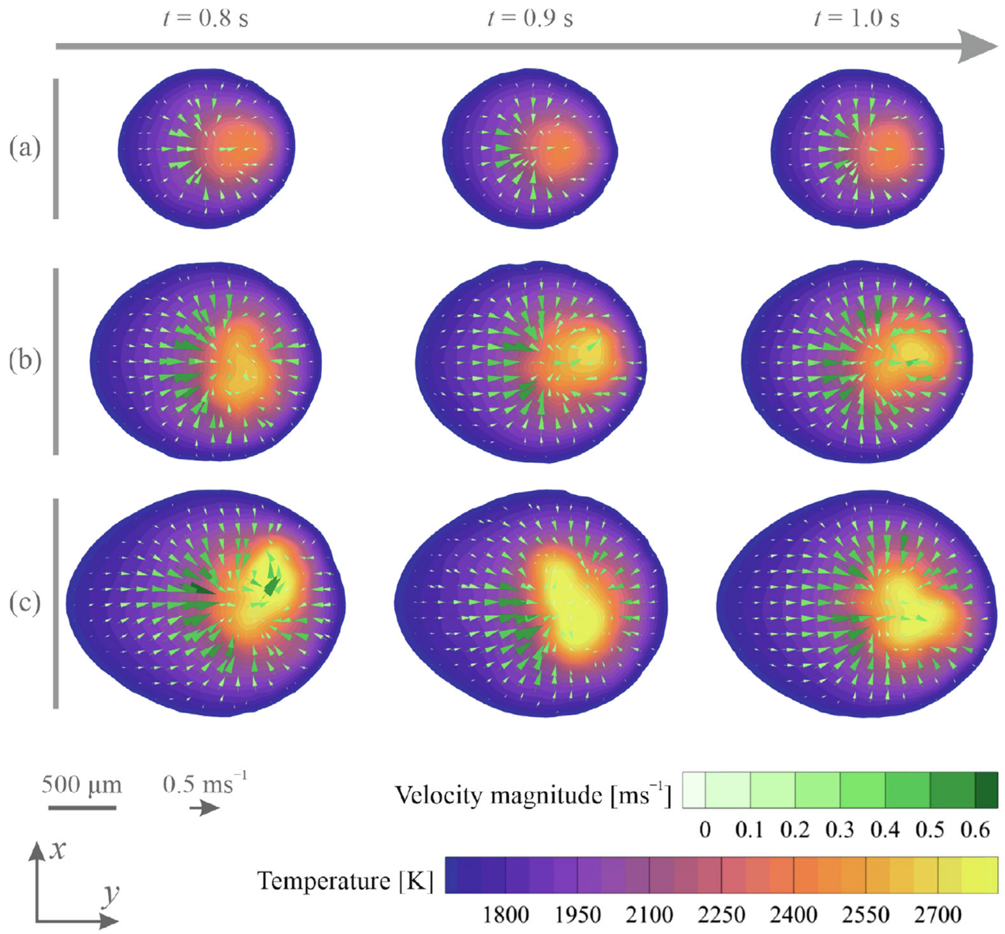

Fig. 10. Evolution of thermal and fluid flow fields over the melt-pool surface during laser melting of stainless steel 316L with different laser powers. (a) $\mathscr{P}$ = 500 W, (b) $\mathscr{P} = 700$ W, and (c) $\mathscr{P}$ = 900 W. The variable absorptivity model is utilised. Cases belong to batch 2, where an Nd:YAG laser ($\lambda = 1.064 \times 10^{-6}$ m) is employed with a travel speed of 10^{-2} m s^{-1}.

that locally deforms the melt-pool surface. Beneath the front part of the depressed region, a relatively thin layer of molten metal exists as shown in Fig. 9. The maximum molten metal velocity over the surface in the depressed region is about 6 m s^{-1} due to the large temperature gradients, forming a multi-cellular flow pattern in the thin molten metal layer due to Marangoni flow instabilities [61]. The maximum molten metal velocity predicted for cases in batch 3 is higher than that for cases in batch 1 and 2. This is primarily attributed to larger temperature gradients induced over the surface, increasing the magnitude of Marangoni shear force. Moreover, for temperatures above a critical value at which the sign of the temperature gradient of surface tension ($\mathrm{d}\gamma/\mathrm{d}T$) changes from positive to negative (see Fig. 2(e)), the absolute value of the temperature gradient of surface tension increases with temperature, increasing the magnitude of Marangoni force applied to the molten material. Due to the recoil pressure and the outward fluid motion on the surface, molten metal accumulates ahead of the depressed region, which is also observed experimentally by Nakamura et al. [62] and simulated numerically by Khairallah et al. [36,1]. Elements of the accumulated liquid volume can be ejected from the pool and form spatters as shown in Fig. 11(a and c). Spatters are small compared to the melt-pool volume and generally cool down during their flight and thus do not have sufficient thermal energy to melt the substrate and stick to the surface. Molten metal moves from the central region of the depressed region towards the melt-pool rim and transfers the heat absorbed from the laser. This fluid velocity corresponds to a Péclet number (Pe) in the order of $\mathscr{O}(100)$, which is similar to the conduction-mode laser melting. Molten metal moving from the depressed region towards the rear part of the pool meets an inward flow in the transition region, resulting in the formation of two vortices over the surface. In the transition region, surface temperature is less than the critical temperature at which the sign of the temperature gradient changes (see Fig. 2(e)), thus the surface tension increases with increasing the temperature (*i.e.* $\mathrm{d}\gamma/\mathrm{d}T > 0$) in the transition region, resulting in a fluid motion from the cold to the hot regions. In the trailing region, temperature gradients are too small to generate significant Marangoni forces to drive the molten metal flow, and thus thermal diffusion dominates the energy transfer.

5. Conclusions

The influence of laser characteristics on internal molten metal flow in laser-beam melting of a metallic substrate was investigated numerically using a high-fidelity three-dimensional model. An enhanced absorption model that accounts for laser emission wavelength, surface temperature, laser-ray incident angle and material composition was utilised in the model, and the results compared with experimental measurements as well as numerical data predicted using a constant absorption model. The physics of complex heat and molten metal flow in laser melting is described for various test cases with different laser powers, laser emission wavelengths, and power-density distributions.

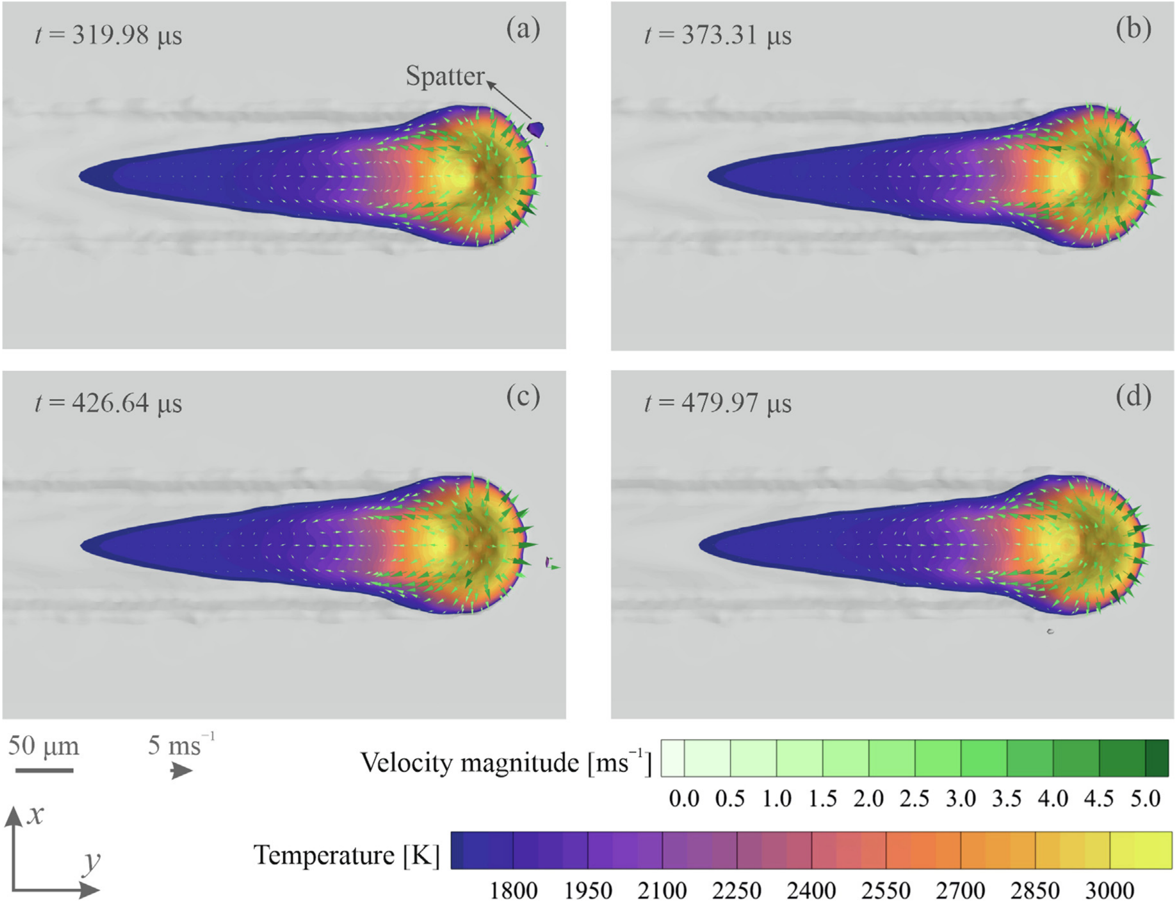

Fig. 11. Evolution of thermal and fluid flow fields over the melt-pool surface during laser melting of stainless steel 316L using a fibre laser ($\lambda = 1.070 \times 10^{-6}$ m) with a laser power of $\mathscr{P}$ = 200 W and a travel speed of 1.5 m s^{-1}. The case belong to batch 3 and the variable absorptivity model is utilised.

For conduction-mode laser melting, where surface deformations are small compared to the melt-pool depth, the absorptivity changes primarily because of changes in surface temperature. However, for cases that surface deformations are significant with respect to the melt-pool depth, changes in the absorptivity are affected by both the surface temperature and the laser-ray incident angle. Changes in the absorptivity affect energy-density distribution over the surface and hence the thermal field over the melt-pool surface, which in turn can influence the Marangoni-driven molten metal flow as well as the distribution of recoil pressure over the surface. These physical processes are tightly coupled to one another, resulting in highly non-linear responses to changes in process parameters.

For laser melting processes with a relatively low power density using a CO_2 or fibre transmissible laser (with an emission wavelength close to 1 µm), the molten metal velocities and surface deformations are relatively small. Because of the small incident angle, the absorptivity for a CO_2 laser is lower than that for a Nd:YAG laser; thus, a lower laser power is required to obtain a melt-pool with similar dimensions using an Nd:YAG laser as compared to a CO_2 laser. Switching to a relatively high power density laser melting process, molten metal velocities increase compared to the low power density processes. For sufficiently high power densities, melt-pool surface deformations become significant, resulting in strongly enhanced laser absorption which in turn further enhances metal vaporisation.

The results of the present work demonstrate that the coupling between these physical processes cannot be rendered with sufficient resolution employing a constant absorptivity model, reducing the range of predictability of the computational models developed to describe the dynamics of melt-pool behaviour in laser welding and additive manufacturing. Moreover, considering absorptivity as a calibration parameter in computational models necessitates trial-and-error simulations, which increases the total costs of computational analyses.

Although the focus of the present work is primarily on laser melting of bare metallic substrates without powder layers, the fundamental laser-matter interaction mechanisms described here are similar to those in laser melting of powder beds. The enhanced laser-absorptivity model employed in the present work can also be utilised in numerical simulations of melt-pool behaviour in laser melting of powder beds, provided that multiple reflections are included in the model.

Author Contributions

Conceptualisation, A.E.; methodology, A.E., M.S., S.J.L.B. and M.L.; software, A.E.; validation, A.E., M.S. and S.J.L.B.; formal analysis, A.E.; investigation, A.E., M.S., S.J.L.B. and M.L.; resources, A.E., M.S., S.J.L.B., M.L., G.R.B.E.R. and M.J.M.H.; data curation, A.E., M.S., S.J.L.B. and M.L.; writing—original draft preparation, A.E.; writing—review and editing, A.E., M.S., S.J.L.B., M.L., G.R.B.E.R., I.M.R., C.R.K. and M.J.M.H.; visualisation, A.E., M.S., S.J.L.B. and M.L.; supervision, G.R.B.E.R., I.M.R., C.R.K. and M.J.M.H.; project administration, A.E., G.R.B.E.R. and M.J.M.H.; and funding acquisition, G.R.B.E.R., I.M.R. and M.J.M.H.

Data availability

The raw/processed data required to reproduce these findings cannot be shared at this time due to their large size, but representative samples of the research data are presented in the paper. Other datasets generated during this study are available from the corresponding author on reasonable request.

Declaration of Competing Interest

The authors declare that they have no known competing financial interests or personal relationships that could have appeared to influence the work reported in this paper.

Acknowledgement

This research was carried out under project numbers F31.7.13504, P16-46/S17024i and P16-46/S17024m in the framework of the Partnership Program of the Materials innovation institute M2i (www.m2i.nl) and the Foundation for Fundamental Research on Matter (FOM) (www.fom.nl), which is part of the Netherlands Organisation for Scientific Research (www.nwo.nl). This research project is also a part of Aim2XL program (www.m2i.nl/aim2xl). The authors would like to thank the industrial partners in this project "Allseas Engineering B.V." and "Rotterdam Fieldlab Additive Manufacturing B.V. (RAMLAB)" for the financial support.

Appendix A. Supplementary material

Supplementary data associated with this article can be found, in the online version, at https://doi.org/10.1016/j.matdes.2022.110385.

References

[1] S.A. Khairallah, A.A. Martin, J.R.I. Lee, G. Guss, N.P. Calta, J.A. Hammons, M.H. Nielsen, K. Chaput, E. Schwalbach, M.N. Shah, M.G. Chapman, T.M. Willey, A.M. Rubenchik, A.T. Anderson, Y.M. Wang, M.J. Matthews, W.E. King, Controlling interdependent meso-nanosecond dynamics and defect generation in metal 3D printing, Science 368 (6491) (2020) 660–665, https://doi.org/10.1126/science.aay7830.

[2] M. Markl, C. Körner, Multiscale modeling of powder bed-based additive manufacturing, Annu. Rev. Mater. Res. 46 (1) (2016) 93–123, https://doi.org/10.1146/annurev-matsci-070115-032158.

[3] A. Ebrahimi, C.R. Kleijn, I.M.A. Richardson, simulation-based approach to characterise melt-pool oscillations during gas tungsten arc welding, Int. J. Heat Mass Transf. 164 (2021) 120535, https://doi.org/10.1016/j.ijheatmasstransfer.2020.120535.

[4] M.M. Francois, A. Sun, W.E. King, N.J. Henson, D. Tourret, C.A. Bronkhorst, N.N. Carlson, C.K. Newman, T. Haut, J. Bakosi, J.W. Gibbs, V. Livescu, S.A.V. Wiel, A.J. Clarke, M.W. Schraad, T. Blacker, H. Lim, T. Rodgers, S. Owen, F. Abdeljawad, J. Madison, A.T. Anderson, J.-L. Fattebert, R.M. Ferencz, N.E. Hodge, S.A. Khairallah, O. Walton, Modeling of additive manufacturing processes for metals: Challenges and opportunities, Curr. Opin. Solid State Mater. Sci. 21 (4) (2017) 198–206, https://doi.org/10.1016/j.cossms.2016.12.001.

[5] T. DebRoy, T. Mukherjee, H.L. Wei, J.W. Elmer, J.O. Milewski, Metallurgy, mechanistic models and machine learning in metal printing, Nat. Rev. Mater. 6 (1) (2020) 48–68, https://doi.org/10.1038/s41578-020-00236-1.

[6] P.S. Cook, A.B. Murphy, Simulation of melt pool behaviour during additive manufacturing: Underlying physics and progress, Addit. Manuf. 31 (2020) 100909, https://doi.org/10.1016/j.addma.2019.100909.

[7] B.J. Simonds, J. Tanner, A. Artusio-Glimpse, P.A. Williams, N. Parab, C. Zhao, T. Sun, The causal relationship between melt pool geometry and energy absorption measured in real time during laser-based manufacturing, Appl. Mater. Today 23 (2021) 101049, https://doi.org/10.1016/j.apmt.2021.101049.

[8] A. Ebrahimi, C.R. Kleijn, I.M. Richardson, Numerical study of molten metal melt pool behaviour during conduction-mode laser spot melting, J. Phys. D: Appl. Phys. 54 (2021) 105304, https://doi.org/10.1088/1361-6463/abca62.

[9] A. Ebrahimi, C.R. Kleijn, M.J.M. Hermans, I.M. Richardson, The effects of process parameters on melt-pool oscillatory behaviour in gas tungsten arc welding, J. Phys. D: Appl. Phys. 54 (27) (2021) 275303, https://doi.org/10.1088/1361-6463/abf808.

[10] J. Xie, A. Kar, J.A. Rothenflue, W.P. Latham, Temperature-dependent absorptivity and cutting capability of CO_2, Nd:YAG and chemical oxygen-iodine lasers, J. Laser Appl. 9 (2) (1997) 77–85, https://doi.org/10.2351/1.4745447.

[11] A. Mahrle, E. Beyer, Theoretical aspects of fibre laser cutting, J. Phys. D: Appl. Phys. 42 (17) (2009) 175507, https://doi.org/10.1088/0022-3727/42/17/175507.

[12] Z. Ren, D.Z. Zhang, G. Fu, J. Jiang, M. Zhao, High-fidelity modelling of selective laser melting copper alloy: Laser reflection behavior and thermal-fluid dynamics, Mater. Des. 207 (2021) 109857, https://doi.org/10.1016/j.matdes.2021.109857.

[13] Z. Yang, A. Bauereiß, M. Markl, C. Körner, Modeling laser beam absorption of metal alloys at high temperatures for selective laser melting, Adv. Eng. Mater. (2021) 2100137, https://doi.org/10.1002/adem.202100137.

[14] Y. Shu, D. Galles, O.A. Tertuliano, B.A. McWilliams, N. Yang, W. Cai, A.J. Lew, A critical look at the prediction of the temperature field around a laser-induced melt pool on metallic substrates, Sci. Rep. 11 (1) (2021), https://doi.org/10.1038/s41598-021-91039-z.

[15] A. Kidess, S. Kenjereš, B.W. Righolt, C.R. Kleijn, Marangoni driven turbulence in high energy surface melting processes, Int. J. Therm. Sci. 104 (2016) 412–422, https://doi.org/10.1016/j.ijthermalsci.2016.01.015.

[16] D. Grange, A. Queva, G. Guillemot, M. Bellet, J.-D. Bartout, C. Colin, Effect of processing parameters during the laser beam melting of Inconel 738: Comparison between simulated and experimental melt pool shape, J. Mater. Process. Technol. 289 (2021) 116897, https://doi.org/10.1016/j.jmatprotec.2020.116897.

[17] A. De, T. DebRoy, A smart model to estimate effective thermal conductivity and viscosity in the weld pool, J. Appl. Phys. 95 (9) (2004) 5230–5240, https://doi.org/10.1063/1.1695593.

[18] W.E. King, A.T. Anderson, R.M. Ferencz, N.E. Hodge, C. Kamath, S.A. Khairallah, A.M. Rubenchik, Laser powder bed fusion additive manufacturing of metals; physics, computational, and materials challenges, Appl. Phys. Rev. 2 (4) (2015) 041304, https://doi.org/10.1063/1.4937809.

[19] S.A. Khairallah, A. Anderson, Mesoscopic simulation model of selective laser melting of stainless steel powder, J. Mater. Process. Technol. 214 (11) (2014) 2627–2636, https://doi.org/10.1016/j.jmatprotec.2014.06.001.

[20] R. Indhu, V. Vivek, L. Sarathkumar, A. Bharatish, S. Soundarapandian, Overview of laser absorptivity measurement techniques for material processing, Lasers Manuf. Mater. Process. 5 (4) (2018) 458–481, https://doi.org/10.1007/s40516-018-0075-1.

[21] J. Ye, S.A. Khairallah, A.M. Rubenchik, M.F. Crumb, G. Guss, J. Belak, M.J. Matthews, Energy coupling mechanisms and scaling behavior associated with laser powder bed fusion additive manufacturing, Adv. Eng. Mater. 21 (7) (2019) 1900185, https://doi.org/10.1002/adem.201900185.

[22] D. Svetlizky, M. Das, B. Zheng, A.L. Vyatskikh, S. Bose, A. Bandyopadhyay, J.M. Schoenung, E.J. Lavernia, N. Eliaz, Directed energy deposition (DED) additive manufacturing: Physical characteristics, defects, challenges and applications, Mater. Today (2021), https://doi.org/10.1016/j.mattod.2021.03.020.

[23] J. Trapp, A.M. Rubenchik, G. Guss, M.J. Matthews, In situ absorptivity measurements of metallic powders during laser powder-bed fusion additive manufacturing, Appl. Mater. Today 9 (2017) 341–349, https://doi.org/10.1016/j.apmt.2017.08.006.

[24] J. Ready, Industrial applications of lasers, second ed., Academic Press, San Diego, 1997. ISBN 9780125839617.

[25] S. Katayama, Handbook of laser welding technologies, Woodhead Publishing Limited, Philadelphia, PA, 2013. ISBN 9780857092649.

[26] N. Kouraytem, X. Li, R. Cunningham, C. Zhao, N. Parab, T. Sun, A.D. Rollett, A.D. Spear, W. Tan, Effect of laser-matter interaction on molten pool flow and keyhole dynamics, Phys. Rev. Appl. 11 (6) (2019) 064054, https://doi.org/10.1103/physrevapplied.11.064054.

[27] A.I. Lvovsky, Fresnel equations, in: Encyclopedia of Optical and Photonic Engineering, second ed., CRC Press, Boca Raton, Florida, 2015. ISBN 9781351247184.

[28] M. Bass, Laser materials processing, Elsevier Science, Amsterdam, North-Holland, 1983, ISBN 9780444863966.

[29] B.J. Simonds, J. Sowards, J. Hadler, E. Pfeif, B. Wilthan, J. Tanner, C. Harris, P. Williams, J. Lehman, Time-resolved absorptance and melt pool dynamics during intense laser irradiation of a metal, Phys. Rev. Appl. 10 (4) (2018) 044061, https://doi.org/10.1103/physrevapplied.10.044061.

[30] K. Ujihara, Reflectivity of metals at high temperatures, J. Appl. Phys. 43 (5) (1972) 2376–2383, https://doi.org/10.1063/1.1661506.

[31] L. Wang, W. Yan, Thermoelectric magnetohydrodynamic model for laser-based metal additive manufacturing, Phys. Rev. Appl. 15 (6) (2021) 064051, https://doi.org/10.1103/physrevapplied.15.064051.

[32] Z.S. Saldi, Marangoni driven free surface flows in liquid weld pools (PhD dissertation), Delft University of Technology, 2012.

[33] A. Jaques, Thermophysical properties of argon. Technical Report FNAL-TM-1517, Illinois, United States, 1988.

[34] K.C. Mills, Fe-316 stainless steel, in: Recommended Values of Thermophysical Properties for Selected Commercial Alloys, Elsevier, 2002, pp. 135–142, https://doi.org/10.1533/9781845690144.135.

[35] T. Heeling, M. Cloots, K. Wegener, Melt pool simulation for the evaluation of process parameters in selective laser melting, Addit. Manuf. 14 (2017) 116–125, https://doi.org/10.1016/j.addma.2017.02.003.

[36] S.A. Khairallah, A.T. Anderson, A. Rubenchik, W.E. King, Laser powder-bed fusion additive manufacturing: Physics of complex melt flow and formation mechanisms of pores, spatter, and denudation zones, Acta Mater. 108 (2016) 36–45, https://doi.org/10.1016/j.actamat.2016.02.014.

[37] C.S. Kim, Thermophysical properties of stainless steels. Technical Report ANL-75-55, Illinois, United States, 1975.

[38] P. Pichler, B.J. Simonds, J.W. Sowards, G. Pottlacher, Measurements of thermophysical properties of solid and liquid NIST SRM 316L stainless steel, J. Mater. Sci. 55 (9) (2019) 4081–4093, https://doi.org/10.1007/s10853-019-04261-6.

[39] P. Sahoo, T. Debroy, M.J. McNallan, Surface tension of binary metal—surface active solute systems under conditions relevant to welding metallurgy, Metall. Trans. B 19 (3) (1988) 483–491, https://doi.org/10.1007/bf02657748.

[40] C.W. Hirt, B.D. Nichols, Volume of fluid (VOF) method for the dynamics of free boundaries, J. Comput. Phys. 39 (1) (1981) 201–225, https://doi.org/10.1016/0021-9991(81)90145-5.

[41] V.R. Voller, C.R. Swaminathan, General source-based method for solidification phase change, Numer. Heat Transf. Part B: Fundam. 19 (2) (1991) 175–189, https://doi.org/10.1080/10407799108944962.

[42] V.R. Voller, C. Prakash, A fixed grid numerical modelling methodology for convection-diffusion mushy region phase-change problems, Int. J. Heat Mass Transf. 30 (8) (1987) 1709–1719, https://doi.org/10.1016/0017-9310(87)90317-6.

[43] A. Ebrahimi, C.R. Kleijn, I.M. Richardson, Sensitivity of numerical predictions to the permeability coefficient in simulations of melting and solidification using the enthalpy-porosity method, Energies 12 (22) (2019) 4360, https://doi.org/10.3390/en12224360.

[44] J.U. Brackbill, D.B. Kothe, C. Zemach, A continuum method for modeling surface tension, J. Comput. Phys. 100 (2) (1992) 335–354, https://doi.org/10.1016/0021-9991(92)90240-y.

[45] S.I. Anisimov, Instabilities in Laser-matter interaction, CRC Press, Boca Raton, Fla, 1995, ISBN 0849386608.

[46] J.Y. Lee, S.H. Ko, D.F. Farson, C.D. Yoo, Mechanism of keyhole formation and stability in stationary laser welding, J. Phys. D: Appl. Phys. 35 (13) (2002) 1570–1576, https://doi.org/10.1088/0022-3727/35/13/320.

[47] K.L. Johnson, T.M. Rodgers, O.D. Underwood, J.D. Madison, K.R. Ford, S.R. Whetten, D.J. Dagel, J.E. Bishop, Simulation and experimental comparison of the thermo-mechanical history and 3D microstructure evolution of 304L stainless steel tubes manufactured using LENS, Comput. Mech. 61 (5) (2017) 559–574, https://doi.org/10.1007/s00466-017-1516-y.

[48] K. Sridharan, T. Allen, M. Anderson, G. Cao, G. Kulcinski, Emissivity of candidate materials for VHTR applicationbs: Role of oxidation and surface modification treatments. Technical report, University of Wisconsin, 2011. URL https://www.osti.gov/biblio/1022709.

[49] R. Ducharme, K. Williams, P. Kapadia, J. Dowden, B. Steen, M. Glowacki, The laser welding of thin metal sheets: an integrated keyhole and weld pool model with supporting experiments, J. Phys. D: Appl. Phys. 27 (8) (1994) 1619–1627, https://doi.org/10.1088/0022-3727/27/8/006.

[50] F. Wooten, Optical properties of solids, Academic Press, New York, 1972, ISBN 1483220761.

[51] Release 19.2. ANSYS Fluent. https://www.ansys.com/.

[52] A. Ebrahimi, C.R. Kleijn, I.M. Richardson, The influence of surface deformation on thermocapillary flow instabilities in low Prandtl melting pools with surfactants, in: Proceedings of the 5th World Congress on Mechanical, Chemical, and Material Engineering. Avestia Publishing, 2019b. https://doi.org/10.11159/htff19.201.

[53] A. Ebrahimi, A. Babu, C.R. Kleijn, M.J.M. Hermans, I.M. Richardson, The effect of groove shape on molten metal flow behaviour in gas metal arc welding, Materials 14 (23) (2021) 7444, https://doi.org/10.3390/ma14237444.

[54] S.V. Patankar, Numerical Heat Transfer and Fluid Flow, first ed., Taylor & Francis Inc, 1980. ISBN 0891165223.

[55] R.I. Issa, Solution of the implicitly discretised fluid flow equations by operator-splitting, J. Comput. Phys. 62 (1) (1986) 40–65, https://doi.org/10.1016/0021-9991(86)90099-9.

[56] O. Ubbink, Numerical Prediction of Two Fluid Systems with Sharp Interfaces (PhD dissertation), Imperial College London (University of London), London, United Kingdom, 1997. URL http://hdl.handle.net/10044/1/8604.

[57] J. Kell, J. Tyrer, R. Higginson, R. Thomson, J. Jones, S. Noden, Holographic diffractive optical elements allow improvements in conduction laser welding of steels, : International Congress on Applications of Lasers & Electro-Optics, Laser Institute of America, 2006. https://doi.org/10.2351/1.5060749.

[58] K.C. Mills, B.J. Keene, R.F. Brooks, A. Shirali, Marangoni effects in welding, Philos. Trans. R. Soc. A: Math. Phys. Eng. Sci. 356 (1739) (1998) 911–925, https://doi.org/10.1098/rsta.1998.0196.

[59] A. Kidess, S. Kenjereš, C.R. Kleijn, The influence of surfactants on thermocapillary flow instabilities in low Prandtl melting pools, Phys. Fluids 28 (6) (2016) 062106, https://doi.org/10.1063/1.4953797.

[60] C.X. Zhao, C. Kwakernaak, Y. Pan, I.M. Richardson, Z. Saldi, S. Kenjeres, C.R. Kleijn, The effect of oxygen on transitional Marangoni flow in laser spot welding, Acta Mater. 58 (19) (2010) 6345–6357, https://doi.org/10.1016/j.actamat.2010.07.056.

[61] M.F. Schatz, G.P. Neitzel, Experiments on thermocapillary instabilities, Annu. Rev. Fluid Mech. 33 (1) (2001) 93–127, https://doi.org/10.1146/annurev.fluid.33.1.93.

[62] H. Nakamura, Y. Kawahito, K. Nishimoto, S. Katayama, Elucidation of melt flows and spatter formation mechanisms during high power laser welding of pure titanium, J. Laser Appl. 27 (3) (2015) 032012, https://doi.org/10.2351/1.4922383.